Deep Learning Initialized and Gradient Enhanced Level-Set Based Segmentation for Liver Tumor From CT Images

YUE ZHANG[1,2,3], (Graduate Student Member, IEEE), **BENXIANG JIANG**[1,4], **JIONG WU**[1,5],
DONGCEN JI[1,4], **YILONG LIU**[2,3], **YIFAN CHEN**[6], (Senior Member, IEEE),
ED X. WU[2,3], (Fellow, IEEE), AND **XIAOYING TANG**[1], (Member, IEEE)

[1]Department of Electrical and Electronic Engineering, Southern University of Science and Technology, Shenzhen 518055, China
[2]Laboratory of Biomedical Imaging and Signal Processing, The University of Hong Kong, Hong Kong
[3]Department of Electrical and Electronic Engineering, The University of Hong Kong, Hong Kong
[4]School of Electronics and Information Technology, Harbin Institute of Technology, Shenzhen 518055, China
[5]School of Electronics and Information Technology, Sun Yat-sen University, Guangzhou 510006, China
[6]School of Life Science and Technology, University of Electronic Science and Technology of China, Chengdu 611731, China

Corresponding author: Xiaoying Tang (tangxy@sustech.edu.cn)

ABSTRACT Liver and liver tumor segmentation provides vital biomarkers for surgical planning and hepatic diagnosis. In this paper, we propose and validate a novel level-set method integrating an enhanced edge indicator and an automatically derived initial curve for CT based liver tumor segmentation. At the preprocessing step, the CT image intensity values were truncated to lie in a fixed range to enhance the image contrast surrounding liver and liver tumor. To remove non-liver tissues for subsequent tumor segmentation, liver was firstly segmented using two convolutional neural networks in a coarse-to-fine manner. A 2D slice-based U-net was used to roughly localize the liver and a 3D patch-based fully convolutional network was used to refine the liver segmentation as well as to roughly localize the liver tumor. A novel level-set method was then presented to further refine the tumor segmentation. Specifically, the probabilistic distribution of the liver tumor was estimated using unsupervised fuzzy c-means clustering, which was then utilized to enhance the edge-detector used in level-set. Effectiveness of the proposed pipeline was validated on two publicly-available datasets. Experimental results identified the superior segmentation performance of the proposed pipeline over state-of-the-art methods.

INDEX TERMS Segmentation, convolutional neural network, liver tumor, level-set, fuzzy c-means.

I. INTRODUCTION

Liver is the largest gland in the human body (approximately 1500 grams) and it is one of the most important metabolic organs of human being with multiple functions, such as metabolism, digestion and detoxification [1]. Liver is vulnerable to many diseases such as hepatic steatosis and hepatitis which are leading causes of hepatic sclerosis and liver tumor. With approximately 841, 080 cases and 781, 631 attributed deaths reported globally in 2018 [2], liver tumor is one of the leading causes of cancer-related deaths. To ablate tumor tissues and leave the surrounding healthy tissues intact, there is

a need for accurately targeting the tumor area [3]. Computed tomography (CT) is one of the most widely used imaging modalities for liver tumor evaluation and staging [4]. Usually, liver and liver tumor segmentations are obtained from experienced radiologists via manual delineation. However, manually tracing volumetric CT images in a slice-by-slice manner is subjective, poorly reproducible, and labor-intensive. Automated or semi-automated segmentation methods would largely improve efficiency. Furthermore, an increased use of intraoperative 3D visualization systems underscores the urgency for automated liver and liver tumor segmentation [5].

In the past decade, various liver segmentation and liver tumor segmentation methods have been developed for CT

The associate editor coordinating the review of this manuscript and approving it for publication was Qichun Zhang.

images. These approaches can be roughly categorized into two classes: model-based methods and deep learning-based methods.

For liver segmentation algorithms, prior anatomical knowledge, such as shape prior, of liver can be incorporated into the segmentation process for model-based methods [6], [7]. However, the computation time of shape-based methods is typically high due to a need for image registration which is computationally demanding. Beichel *et al.* presented a 3D interactive liver segmentation pipeline using graph cut [8], [9]. Susomboon *et al.* employed a hybrid method by jointly using expectation maximization algorithm and region-based texture classification [10]. These techniques may nevertheless fail to separate liver and neighboring tissues due to low contrast and fuzzy boundaries. Moreover, contrast material is usually used to clearly visualize tumor, which will bring noise in CT images [11]. Recently, deep learning approaches, especially fully convolutional networks (FCNs), have shown remarkable potential in automatic medical image segmentation [12]–[14]. Dou *et al.* proposed a novel and efficient 3D FCN for volumetric medical image segmentation, with application to liver [15]. The accuracy of automated liver segmentation using deep learning has been reported to be over 95% in terms of Dice score [16]–[18], which is very accurate and has a great potential to be used in clinical applications.

Nevertheless, automated liver tumor segmentation is very challenging due to the very fuzzy boundaries between tumorous tissues and healthy tissues. And no prior knowledge can be applied because of tumor's wide variabilities in terms of size, shape, and location [19]. To tackle this challenge, various liver tumor segmentation algorithms have been designed. For instance, Goetz *et al.* proposed a two-stage method, wherein liver was segmented firstly using shape models, and then tumor segmentation was achieved using randomized trees with an auto-context learning scheme [20]. Häme *et al.* presented a semi-automatic tumor segmentation scheme based on non-parametric intensity distribution estimation and a hidden Markov field model [21]. These methods generally suffer from low accuracy and significantly high computation cost. Among model-based techniques, level-set methods (LSMs) are widely used because they can combine image information and model properties [22]–[26]. A novel LSM combining likelihood energy with edge energy was proposed by Li *et al.* [23], which performed better than the traditional Chan-Vese model [27] and the geodesic LSM [28]. Smeets *et al.* incorporated fuzzy pixel classification into an edge-based LSM for liver tumor segmentation [29]. The main limitations of these methods are that they need manually-created initial regions of interest (ROIs), and there is still room for improvement in terms of segmentation accuracy. Recently, deep learning has been applied in liver tumor segmentation from CT images [30]–[34]. For example, Li *et al.* proposed a novel H-DenseUNet by combining a 2D U-net and a 3D convolutional neural network (CNN) [16]. Seo *et al.* proposed a modified U-net by adding a residual path to the skip connection parts of U-net [33]. Jiang *et al.* presented

a CNN structure making use of attention mechanism and skip connections [34]. The main limitation of deep learning techniques is that they do not incorporate domain knowledge and may suffer uninterpretable segmentation errors. A recent research trend is to combine deep learning methods and domain knowledge driven methods such as LSMs [35]. Deep learning may be helpful in providing the initial ROIs needed by LSMs, and LSMs may further improve the accuracy and topology integrity of deep learning based segmentation results. In addition, the performance of edge-based LSMs largely relies on the prerequisite that liver tumor has clear and differentiating boundaries. As such, edge enhancing is very crucial for LSMs, especially in CT image based liver tumor segmentation.

To address the aforementioned issues, we proposed a novel LSM with an automatically-defined initial ROI and an enhanced edge indicator for liver tumor segmentation. A 2D U-net and a 3D FCN were sequentially used for a coarse-to-fine liver segmentation which was then used to mask out non-liver tissues. A coarse liver tumor segmentation was also obtained from the 3D FCN, which was then used to initialize the subsequent distance regularized level-set evolution (DRLSE) [24]. Furthermore, we employed fuzzy c-means (FCM) [36] to estimate the probability that a pixel belongs to a certain image class (tumor or non-tumor) and used that probabilistic mask to enhance the edge indicator used in the proposed LSM. A key strength of this study is the combination of a data-driven method (deep learning) and model-driven methods (level-set and FCM).

The rest of this paper is arranged as follows. The flowchart of the proposed method is depicted in section II, and the three key components (data processing procedures, deep learning-based segmentation and FCM-based LSM) are detailed. The datasets and evaluation criteria on assessing the segmentation performance are shown in section III. Evaluations of the proposed method are presented in section IV. Finally, section V discusses advantages and potential limitations of the proposed pipeline.

II. METHOD

For image preprocessing, we truncated the image intensity values of all CT scans to lie in a fixed range to remove irrelevant details and to enhance the image contrast. For liver segmentation, we employed a coarse-to-fine strategy to reduce computation time as well as to improve segmentation accuracy, which has also been adopted in many other segmentation tasks [37], [38]. For liver tumor segmentation, we adopted a gradient enhanced LSM making use of FCM.

A. IMAGE PREPROCESSING USING INTENSITY TRUNCATION

In CT image reconstruction, quantitative measurements of the tissue density are accomplished using the Hounsfield unit (HU) scale, which measures the x-ray absorption characteristics of the tissue and is linearly related to tissue's mass density [39]. At standard pressure and temperature (STP),
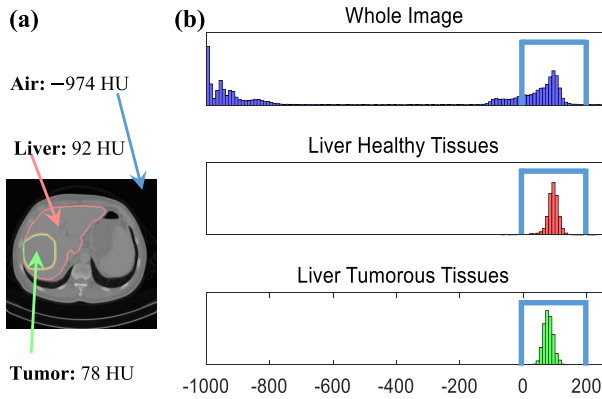
(a) **(b)**

FIGURE 1. CT image intensity analysis for different ROIs.

FIGURE 2. A representative CT slice before and after image intensity truncation using a fixed range [0, 200].

the radiodensity of distilled water is defined as 0 HU, whereas the radiodensity of air is defined as -1000 HU. As such, for a voxel with an average linear attenuation coefficient μ, its corresponding HU value h is given by

$$h = 1000 \times \frac{\mu - \mu_{\text{water}}}{\mu_{\text{water}} - \mu_{\text{air}}}. \qquad (1)$$

The intensity of a CT image i is a linear transformation of h, which is given by

$$i = \frac{h - \text{intercept}}{\text{slope}}, \qquad (2)$$

where "intercept" and "slope" are 0 and 1 for all datasets used in this study. In this context, the voxel's average HU value equals to the intensity of a voxel ($h = i$). On typical medical-grade CT scans, the Hounsfield scale of liver is 60 ± 6 HU at STP [40]. In a real clinical environment, the mean Hounsfield scales of liver will be slightly shifted due to changes in pressure and temperature. In addition, the Hounsfield scale of liver tissues follows a normal distribution because of random noises. Using a normal distribution to fit liver's intensity of each training image, we obtain mean values ranging between 80.23 and 128.20 and standard deviation values ranging between 13.85 and 26.47. This agrees with the theoretically suggested value of 60. To accommodate image variability with the same "intercept" and "slope" values, we use the mean $\pm$ 3std rule, wherein the minimum value and maximum value are respective 18.04 and 201.76. As such, we use [0, 200] for intensity truncation. For datasets used in this work, [0, 200] is large enough to cover all liver tissues, including both healthy tissues and tumorous ones, a representative slice of which is shown in Fig. 1. For CT scans obtained from scanners whose "intercept" and "slope" imaging parameters are not 0 or 1, we can use similar procedures, making use of the relationship between Hounsfield scale and CT image intensity and intensity fitting of training data with the same imaging parameters, to get an appropriate range for intensity truncation.

With the same imaging parameters, the intensity value range of CT images is identical for the same organ, across different subjects [41]. As such, we truncate the image intensity
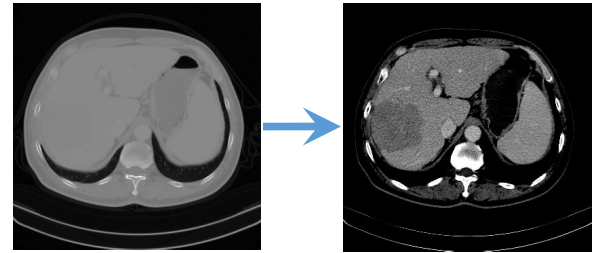
to be within a single fixed range [0, 200] for all CT images. As shown in Fig. 2, the boundaries of both liver and liver tumor are clearer after the aforementioned image preprocessing.

B. LIVER AND LIVER TUMOR SEGMENTATION USING DEEP LEARNING

For CT scanns, both image size and voxel size vary from sample to sample, and spatially inconsistent data are not ideal for deep learning approaches. Previous coarse-fo-fine works [38] suggest the effectiveness of using a coarsely predicted segmentation mask to make the inputs to CNNs have the same image size and the same pixel size. As such, we firstly segment liver using a 2D U-net and define a liver ROI, and then use a 3D FCN to refine the liver segmentation and to segment liver tumor within the liver ROI. The flowchart of our coarse-to-fine pipeline for liver and liver tumor segmentation is shown in Fig. 3.

1) NETWORK ARCHITECTURE

The detailed parameters of 2D U-net and 3D FCN used in this work are listed in Table 1. Both our 2D and 3D CNN models have an encoder-decoder structure with skip connection. The 2D U-net is composed of 9 convolution blocks and each block consists of two 3×3 convolution layers followed by a batch normalization layer (BN) and a rectified linear unit (ReLU). The 3D FCN is composed of 7 convolution blocks, 3 max-pooling layers, and 3 up-sampling layers. The pooling layer and up-sampling layer of 3D FCN is one less than 2D U-net because the input size of 3D FCN is smaller. That is also the reason why fewer feature channels are used in 3D FCN. The number of feature channels is doubled/halved at each downsampling/upsampling step.

2) TRAINING

At the training stage, we conduct two-fold normalizations for the 3D CT image **I** and the corresponding ground truth segmentation **Y**. On the one hand, we divide each 3D volume (**I** and **Y**) into a set of 2D slices and resize them to be of a fixed image size 256×256. These normalized 2D images and ground truth pairs are then fed into a 2D U-net to fit a coarse segmentation model, which focuses on learning discriminative features for liver versus background discrimination. As such, we treat liver tumor as part of
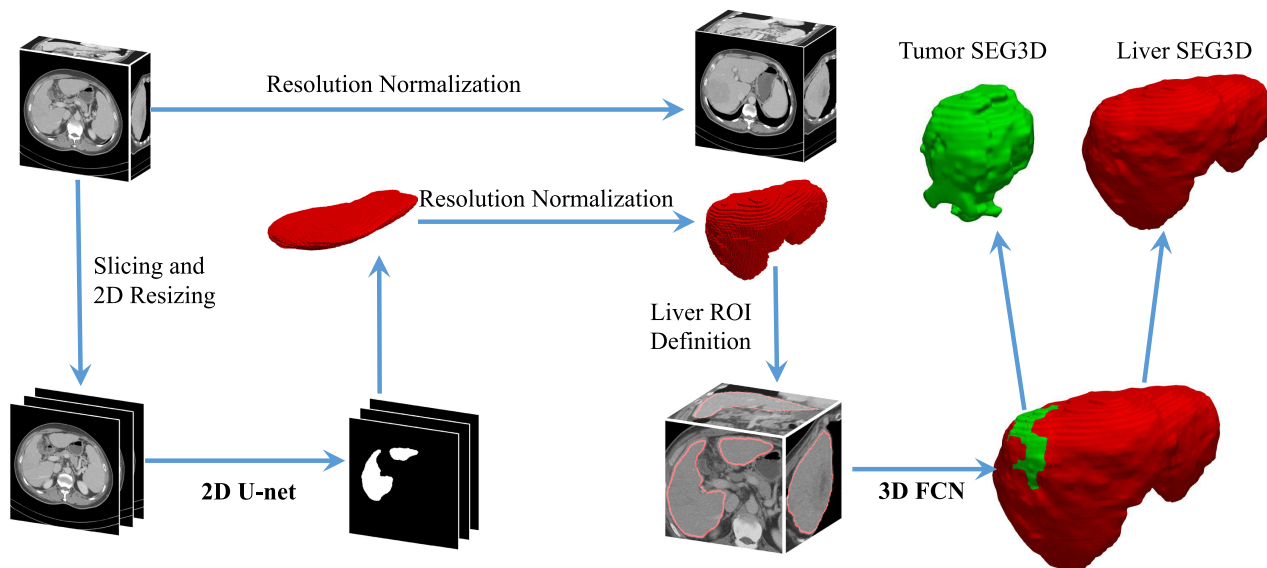
FIGURE 3. Illustration of our coarse-to-fine pipeline for liver and liver tumor segmentation.

TABLE 1. Parameters of the 2D U-net and 3D FCN.

| | 2D U-net | | 3D FCN | |
	Feature size	Parameters	Feature size	Parameters
input	$256 \times 256 \times 1$	-	$48 \times 48 \times 48 \times 1$	-
convolution 1	$256 \times 256 \times 64$	$[3 \times 3, 64 \text{ conv}] \times 2$ [a]	$48 \times 48 \times 48 \times 32$	$[3 \times 3 \times 3, 32 \text{ conv}] \times 2$
pooling	$128 \times 128 \times 64$	$[2 \times 2 \text{ max pool}]$	$24 \times 24 \times 24 \times 32$	$[2 \times 2 \times 2, \text{ max pool}]$
convolution 2	$128 \times 128 \times 128$	$[3 \times 3, 128 \text{ conv}] \times 2$	$24 \times 24 \times 24 \times 64$	$[3 \times 3 \times 3, 64 \text{ conv}] \times 2$
pooling	$64 \times 64 \times 128$	$[2 \times 2 \text{ max pool}]$	$12 \times 12 \times 12 \times 64$	$[2 \times 2 \times 2, \text{ max pool}]$
convolution 3	$64 \times 64 \times 256$	$[3 \times 3, 256 \text{ conv}] \times 2$	$12 \times 12 \times 12 \times 128$	$[3 \times 3 \times 3, 128 \text{ conv}] \times 2$
pooling	$32 \times 32 \times 256$	$[2 \times 2 \text{ max pool}]$	$6 \times 6 \times 6 \times 128$	$[2 \times 2 \times 2, \text{ max pool}]$
convolution4	$32 \times 32 \times 512$	$[3 \times 3, 512 \text{ conv}] \times 2$	-	-
pooling	$16 \times 16 \times 512$	$[2 \times 2 \text{ max pool}]$	-	-
convolution 5	$16 \times 16 \times 512$	$[3 \times 3, 1024 \text{ conv}], [3 \times 3, 512 \text{ conv}]$	$6 \times 6 \times 6 \times 128$	$[3 \times 3 \times 3, 256 \text{ conv}], [3 \times 3 \times 3, 128 \text{ conv}]$
upsampling	$32 \times 32 \times 1024$	$[2 \times 2 \text{ upsampling}]\text{-}[\text{convolution 4}]$ [b]	$12 \times 12 \times 12 \times 256$	$[2 \times 2 \times 2 \text{ upsampling}]\text{-}[\text{convolution 3}]$
convolution 6	$32 \times 32 \times 256$	$[3 \times 3, 512 \text{ conv}], [3 \times 3, 256 \text{ conv}]$	$12 \times 12 \times 12 \times 64$	$[3 \times 3 \times 3, 128 \text{ conv}], [3 \times 3 \times 3, 64 \text{ conv}]$
upsampling	$64 \times 64 \times 512$	$[2 \times 2 \text{ upsampling}]\text{-}[\text{convolution 3}]$	$24 \times 24 \times 24 \times 128$	$[2 \times 2 \times 2 \text{ upsampling}]\text{-}[\text{convolution 2}]$
convolution 7	$64 \times 64 \times 128$	$[3 \times 3, 256 \text{ conv}], [3 \times 3, 128 \text{ conv}]$	$24 \times 24 \times 24 \times 32$	$[3 \times 3 \times 3, 64 \text{ conv}],[3 \times 3 \times 3, 32 \text{ conv}]$
upsampling	$128 \times 128 \times 256$	$[2 \times 2 \text{ upsampling}]\text{-}[\text{convolution 2}]$	$48 \times 48 \times 48 \times 64$	$[2 \times 2 \times 2 \text{ upsampling}]\text{-}[\text{convolution 1}]$
convolution 8	$128 \times 128 \times 64$	$[3 \times 3, 128 \text{ conv}], [3 \times 3, 64 \text{ conv}]$	$48 \times 48 \times 48 \times 16$	$[3 \times 3 \times 3, 32 \text{ conv}], [3 \times 3 \times 3, 16 \text{ conv}]$
upsampling	$256 \times 256 \times 128$	$[2 \times 2 \text{ upsampling}]\text{-}[\text{convolution 1}]$	-	-
convolution 9	$256 \times 256 \times 32$	$[3 \times 3, 64 \text{ conv}], [3 \times 3, 32 \text{ conv}]$	-	-
output	$256 \times 256 \times 1$	$[1 \times 1, 1] + \text{Sigmoid}$	$48 \times 48 \times 48 \times 1$	$[1 \times 1 \times 1, 1] + \text{Sigmoid}$

[a] "3×3, 64 conv" corresponds to a Conv-BN-ReLU layer with a kernel size of 3×3 and 64 features. "[ ]$\times d$" denotes that the convolution block is repeated for d times.
[b] [ ]-[ ] denotes concatenation of two feature maps.

liver in this binary coarse segmentation. On the other hand, we resize each 3D volume (**I** and **Y**) to be of a fixed voxel size $1 \times 1 \times 1$ mm^3 and crop these normalized images using the liver mask. We adopt a dense training strategy to fit a fine segmentation model [42]. Specifically, we train the 3D FCN for 30 epochs, with each one again composed of 20 subepochs. At each subepoch, a total of 100 samples with a size of $48 \times 48 \times 48$ are randomly selected from the training images and the corresponding ground truth segmentation images. The fine liver segmentation stage is conducted with tumor labels and is used to predict a fine liver segmentation and meanwhile to provide a coarse tumor segmentation.

3) TESTING
As shown in Fig. 3, liver is segmented out in a coarse-to-fine manner at the testing stage. At the beginning, we also conduct two-fold image normalizations, the same as that at the training stage. On the one hand, we slice and resize the 3D testing CT image to 2D slices and use the trained U-net to predict a coarse liver segmentation. On the other hand, we resize both the 3D CT image and the coarse liver segmentation to be of the normalized voxel size and crop the resized CT image surrounding the resized coarse liver segmentation. Then the trained 3D FCN is used to yield a fine liver segmentation and a coarse liver tumor segmentation within the cropped CT image.
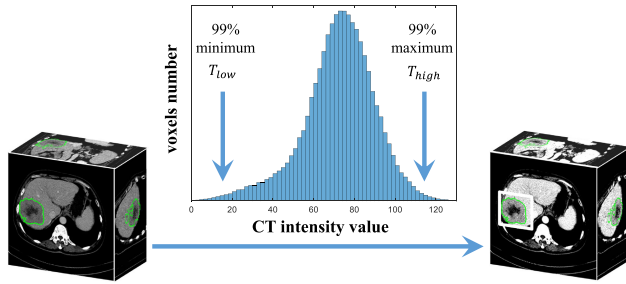
FIGURE 4. A representative example to demonstrate intensity truncation based on a range computed from the coarse tumor segmentation from 3D FCN.

C. LIVER TUMOR SEGMENTATION BASED ON LEVEL-SET

Given the CNN-derived coarse liver tumor segmentation, we obtain histogram statistics for the CT image intensity within the liver tumor and then use the 99th percentile maximum and minimum (T_{low} and T_{high}) to reduce noisy segmentation. A piecewise linear transformation is used to normalize image intensity via

$$y = \begin{cases} 0, & x < T_{low} \\ \dfrac{x - T_{low}}{T_{high} - T_{low}}, & T_{low} < x < T_{high} \\ 1, & x > T_{high}. \end{cases} \quad (3)$$

As shown in Fig. 4, such truncation and normalization can further enhance the image contrast surrounding liver tumor.

We then crop the testing CT image based on an enlarged version of the coarse tumor segmentation (enlarged by 20 pixels at each direction), and then remove non-liver tissues using the fine liver segmentation. Afterwards, we refine tumor segmentation in a slice-by-slice manner as shown in Fig. 5. Let I be a 2D cropped CT image defined on a domain Ω. An implicit contour representation of the tumor can be formed with the zero level-set $\mathcal{C} = \{x \in \Omega | \phi(x) = 0\}$, where points inside the contour have $\phi(x) < 0$ and outside have $\phi(x) > 0$. For a level-set function $\phi : \Omega \to \mathbb{R}$ [24], the energy function $\varepsilon(\phi)$ is defined as

$$\varepsilon(\phi) = \mu \mathcal{R}_p + \lambda \mathcal{L}_g(\phi) + \alpha \mathcal{A}_g(\phi), \quad (4)$$

where $\mathcal{R}_p(\phi) \triangleq \int_\Omega \frac{1}{2}(|\nabla\phi| - 1)^2 \, dx$ is a regularization term that guarantees $|\nabla\phi| \approx 1$, and the length term $\mathcal{L}(\phi) = \int_\Omega g\delta(\phi)|\nabla\phi|dx$ computes the line intergral of the function g along the zero level contour (g is an edge indicator function for I and δ is the Dirac delta function). The area term is computed as $\mathcal{A}(\phi) = \int_\Omega gH(-\phi)dx$ (H is the Heaviside function).

1) ENHANCED OBJECT INDICATION FUNCTION

In order to rectify ambiguous boundaries, we make use of an enhanced object indication function via

$$g_{max} = \max(g_i, g_p). \quad (5)$$

The first term g_i is a normalized edge indicator [24] obtained by

$$g_i = \frac{g(I) - \min(g(I))}{\max(g(I)) - \min(g(I))},$$
$$g(I) = \frac{1}{1 + |\nabla G_\sigma * I|}. \quad (6)$$

The values of g_i range from 0 to 1. G_σ is a Gaussian kernel with a standard deviation σ [44], [45]. The second term g_p is obtained from prior knowledge on I using unsupervised FCM. FCM is an iterative clustering algorithm that can produce C partitions by minimizing an objective function J,

$$J = \sum_{n=1}^{N} \sum_{j=1}^{C} u_{nj}^m ||I_n - c_j||^2$$

$$\text{subject to} \sum_{i=1}^{c} u_{nj} = 1, \quad (7)$$

where m is any real number that is greater than 1, u_{nj} is the degree of membership of I_n in cluster j, I_n is the intensity value of the nth pixel flattened from the 2D CT image I, c_j denotes the intensity center of the corresponding cluster, and $|| \cdot ||$ is the Euclidean distance.

Details of FCM are described in **Algorithm 1**.

Algorithm 1 The Fuzzy C-Means Algorithm

Input: Flattened CT image within liver mask $[I_n]$;
Output: $U^t = [u_{nj}]$;
Fix numberOfClusters $= C$;
Fix maxIteration $= T$;
Fix deltaValue $= \epsilon$;
Randomly initialize U^0;
for $t = 1$ **to** T **do**
  Update elements of membership matrix u_{nj} using

$$u_{nj} = \frac{1}{\sum_{k=1}^{C}(\frac{||I_n - c_j||}{||I_n - c_k||})^{\frac{2}{m-1}}};$$

  Calculate the new cluster centers $[c_j]$ using

$$c_j = \frac{\sum_{i=1}^{N} u_{nj}^m \cdot I_n}{\sum_{i=1}^{N} u_{nj}^m};$$

  Calculate the new objective function J^t using Eq. (7).
  if $|J^t - J^{t-1}| < \epsilon$ **then**
    Break;
  else
    Continue;
  end if
end for

Afterwards, the row of U^t relating to tumor is reshaped to U^{reshape} according to the size and none-zero index of I. An example of U^{reshape} is shown in Fig. 5. We then use the Canny edge detector to detect edges in U^{reshape} and denote the result as g_p.
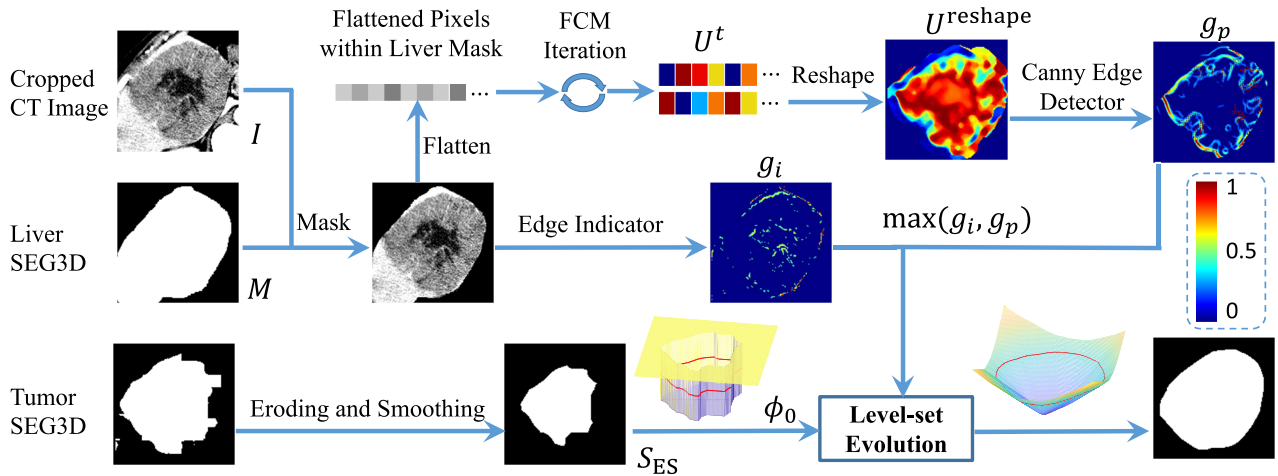
FIGURE 5. Flowchart of liver tumor segmentation using level-set.

2) AUTOMATIC INITIALIZATION

A LSM is sensitive to the initial position of the zero level-set contour. Different from previous semi-automatic methods [19], [29], we use the 3D FCN derived tumor segmentation to be our initial curve in LSM. In a typical edge-based LSM, the balloon force term $\alpha \mathcal{A}_g(\phi)$ either "expands" or "shrinks" the dynamic interface. In this study, we choose the "expands" mode. As such, we erode our coarse tumor segmentation result to get a smaller region. Then a median filter is used to smooth the segmentation and the result is denoted as S_{ES}. The initial function ϕ_0 in our level-set is defined as a binary function,

$$\phi_0(x) = \begin{cases} -c_0, & \text{if } S_{ES} = 1 \\ c_0, & \text{otherwise.} \end{cases} \quad (8)$$

D. IMPLEMENTATION DETAILS

The proposed neural networks were implemented based on Python. All experiments were conducted on a workstation equipped with NVIDIA GTX 1080 Ti. The 2D U-net was trained with a batch size of 8 and the 3D FCN was trained with a batch size of 16. The level-set and FCM parts were implemented using MATLAB.[1,2] The weights in Eq. (4) were the same as those suggested in Li's work [24], wherein $\mu = 0.1$, $\lambda = 1.5$, $\alpha = -1.5$. The level-set evolution stops when it meets the steady solution of the gradient flow equation. We used FCM to distinguish tumor and healthy liver tissues within the liver region. As such, the number of cluster centers C in FCM was set to be 2. The max number of iterations T and the termination criterion in FCM ϵ were respectively set to be 10 and 0.001 empirically.

III. DATASETS AND EVALUATION CRITERIA

A. DATASETS

We test the proposed method on two publicly-available datasets. The first dataset used in this study come from a liver

CT image segmentation challenge on the 2019 International Symposium on Image Computing and Digital Medicine.[3] There are 24 training images and 36 testing images, with varied image sizes and a fixed resolution of $1 \times 1 \times 5$ mm[3]. The second dataset come from the MICCAI 2017 Liver Tumor Segmentation (LiTS) Challenge,[4] which consists of 131 training images and 70 testing images, with varied image sizes and resolution.

B. EVALUATION CRITERIA

1) DICE SIMILARITY COEFFICIENT (DSC)

DSC is the most widely used evaluation metric to quantify the performance of medical image segmentation. It is defined as

$$\text{DSC}(G, R) = \frac{2|G \cap R|}{|G| + |R|}, \quad (9)$$

where R denotes an automated segmentation result, G denotes the corresponding ground truth segmentation, and $G \cap R$ denotes the overlap between G and R. The operator $|\cdot|$ returns the number of pixels (or voxels in 3D) contained in a region which is proportional to the physical volume of the considered region.

2) VOLUMETRIC OVERLAP ERROR (VOE)

Jaccard similarity coefficient (another similarity ratio) is defined as

$$\text{Jaccard}(G, R) = \frac{|G \cap R|}{|G \cup R|}, \quad (10)$$

and volumetric overlap error (VOE) is defined as the corresponding error measure [43]

$$\text{VOE}(G, R) = 1 - \frac{|G \cap R|}{|G \cup R|}. \quad (11)$$

3) RELATIVE VOLUME DIFFERENCE (RVD)

To quantify the volume difference between two binary segmentation, RVD is defined as

$$\text{RVD}(G, R) = \frac{|V_G - V_R|}{V_G}, \quad (12)$$

where V_G and V_R respectively denote the volumes of the ground truth segmentation and the corresponding automated segmentation.

4) AVERAGE AND ROOT MEAN SQUARE OF SYMMETRIC SURFACE DISTANCE (ASD AND RMSD)

Let $S(A)$ denote the set of surface vertices of a 3D volume A, the shortest distance of any vertex v to $S(A)$ is defines as

$$d(v, S(A)) = \min_{s_A \in S(A)} ||v - s_A||, \quad (13)$$

where $|| \cdot ||$ denotes the Euclidean distance, with a greater value indicating a higher error.

The average symmetric surface distance (ASD) [46] between G and R is then defined as

$$\begin{aligned} &\text{ASD}(G, R) \\ &= \frac{1}{|S(G)| + |S(R)|} \\ &\times \left(\sum_{s_G \in S(G)} d(s_G, S(R)) + \sum_{s_R \in S(R)} d(s_R, S(G)) \right), \quad (14) \end{aligned}$$

and the root mean square of the symmetric surface distance (RMSD) is given by

$$\begin{aligned} &\text{RMSD}(G, R) \\ &= \sqrt{\frac{1}{|S(G)| + |S(R)|}} \\ &\times \sqrt{\sum_{s_G \in S(G)} d^2(s_G, S(R)) + \sum_{s_R \in S(R)} d^2(s_R, S(G))}, \quad (15) \end{aligned}$$

where $|S(G)|$ and $|S(R)|$ return the sum of surface area of G and R. The evaluation code for ASD and RMSD is available at Github.[5]

IV. EXPERIMENTS AND RESULTS

Below, section IV-A and section IV-B summarize results obtained from the ISICDM dataset and section IV-C presents results obtained from the LiTS dataset. For both datasets, the training data have manual annotations, but the ground truth segmentations for the testing data are hidden. For the validation experiment in section IV-A, we conducted a 3-fold cross-validation on the training data. For the testing experiment in either section IV-B or section IV-C, we trained a model using the training data and then evaluated the proposed model on the testing data.

[5]https://github.com/deepmind/surface-distance

TABLE 2. Quantitative statistics of 2D U-net and 2D U-net + 3D FCN in terms of liver segmentation based on 3-fold cross-validation. ↓ indicates that a smaller value suggests a better performance.

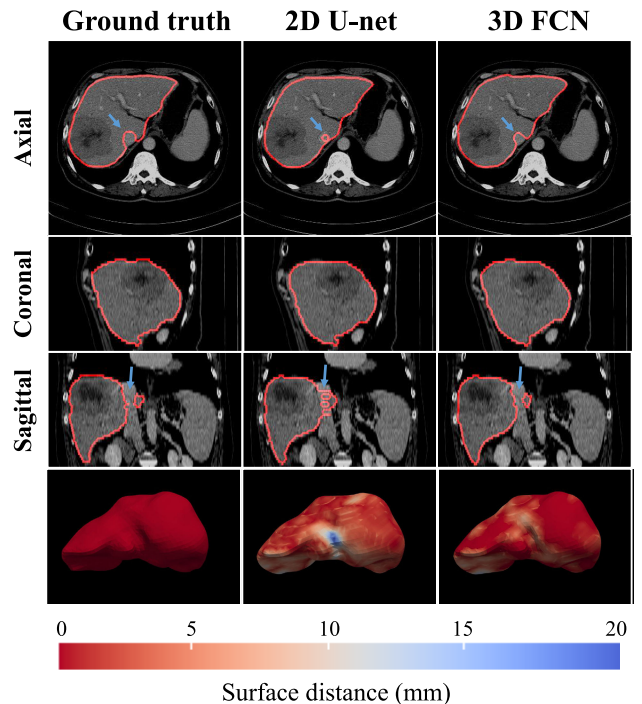|	2D U-net	2D U-net + 3D FCN	p-value
DSC	94.45%± 1.82%	**96.31% ± 0.62%**	0.0001
VOE↓	10.37% ± 3.17%	**8.59% ± 2.21%**	0.0024
RVD↓	3.37% ± 3.26%	**1.62% ± 1.70%**	0.0056
ASD↓	1.29 mm ± 0.84 mm	**0.91 mm ± 0.30 mm**	0.0195
RMSD↓	2.81 mm ± 1.18 mm	**1.99 mm ± 0.64 mm**	0.0005

FIGURE 6. Representative liver segmentation results at each of the three planes from 2D U-net and the proposed 2D U-net + 3D FCN on an ISICDM validation sample.

A. RESULTS OF ISICDM VALIDATION DATASET

1) LIVER SEGMENTATION

Table 2 compares the liver segmentation performance of 2D U-net (coarse stage) and 2D U-net + 3D FCN (fine stage). For each metric, a Wilcoxon signed-rank test is performed to quantify the significance of each group comparison difference. The average DSC of the fine liver segmentation is 96.31%, which is significantly higher than that obtained from the coarse stage (p < 0.01). For all other four evaluation metrics, VOE, RVD, AVD, and RMSD, there are significant decreases from 2D U-net to 2D U-net + 3D FCN. These improvements may have been due to the reason that the 3D model is able to capture spatial and contextual information but the 2D model can only capture information in the axial plane. As shown in Fig. 6, for certain cases, the boundaries between liver and neighboring tissues are much clearer on other planes, such as the sagittal plane, than the axial plane. For those cases, the 2D U-net that solely relies on axial plane

TABLE 3. Quantitative statistics of 3D FCN and 3D FCN followed by level-set (3D FCN + Level-set) in terms of liver tumor segmentation based on 3-fold cross-validation. ↓ indicates that a smaller value suggests a better performance.

	3D FCN	3D FCN + Level-set	p-value
DSC	66.76% ± 17.64%	**72.45% ± 13.42%**	0.0276
VOE↓	47.38% ± 19.08%	**40.77% ± 14.79%**	0.0113
RVD↓	49.76% ± 37.89%	**25.89% ± 21.00%**	0.0087
ASD↓	5.65 mm ± 3.20 mm	**3.04 mm ± 1.18 mm**	0.0035
RMSD↓	10.91 mm ± 8.69 mm	**4.99 mm ± 2.18 mm**	0.0073

images may perform much worse than the proposed 2D U-net + 3D FCN.

Both quantitative and qualitative analyses suggest that our automated liver segmentations are reliable and can be used to effectively mask out non-liver tissues. Please note we firstly used a 2D U-net to roughly localize liver rather than a 3D FCN to directly act on the whole image. This coarse-to-fine strategy is efficient in reducing the computation time since only a smaller number of patches need to be predicted within the cropped CT image. Besides, this strategy is also useful in improving the segmentation accuracy [47].
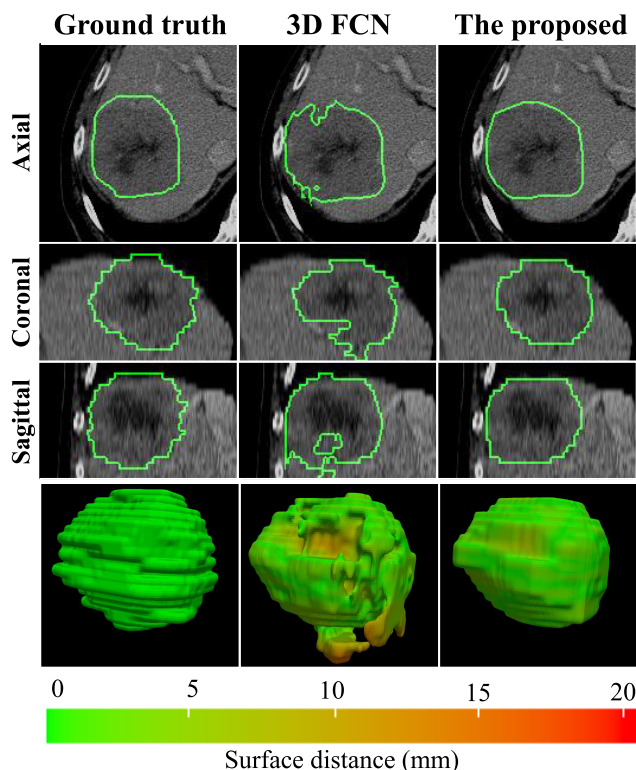
2) TUMOR SEGMENTATION

Compared with 3D FCN, the proposed method (FCN + level-set) achieved 5.69% and 6.61% improvements on tumor segmentation in terms of DSC and VOE, which are both statistically significant (p < 0.05). The segmentation error has been reduced by nearly half in terms of RVD, ASD, and RMSD. Also, the relatively smaller standard deviations indicate that the proposed method is more stable and more robust. This clearly shows the effectiveness of our liver tumor segmentation framework. Detailed comparisons are shown in Table 3.

Fig. 7 shows qualitative comparisons among the ground truth, the automated segmentation results from 3D FCN, and those from the proposed pipeline, for a representative case from ISICDM's validation dataset, at each of the three 2D planes. The improvements may be due to the pipeline's capabilities in restoring missing parts and removing residual parts. The last row in that figure demonstrates the surface rendering comparison results for that specific case in terms of the shortest distance map. Specifically, the color bar in Fig. 7 denotes the shortest distance between each vertex of the automatically-segmented surface and the ground truth surface. The superiority of the proposed tumor segmentation pipeline can be easily observed.

B. RESULTS OF ISICDM TESTING DATA

It may be more meaningful to verify the segmentation performance on testing data the ground truth of which is unavailable. As shown in Fig. 8, the proposed method can deliver highly accurate and much smooth liver tumor segmentations.

FIGURE 7. Examples of tumor segmentation results by 3D FCN and the proposed 3D FCN + level-set on the validation dataset of ISICDM. The last row shows the surface rendering comparison results. The color bar denotes the localized shortest distance to the ground truth surface.

TABLE 4. DSC comparisons of the proposed method and representative state-of-the-art methods on liver and liver tumor segmentation obtained on the LiTS testing dataset.

| Method	Tumor		Liver	
	Dice per case	Dice global	Dice per case	Dice global
The proposed	71.8%	**84.1%**	**96.3%**	**96.7%**
Li *et al.* [16]	**72.2%**	82.4%	96.1%	96.5%
Vorontsov *et al.* [17]	66.1%	78.3%	95.1%	95.1%
Yuan *et al.* [18]	65.7%	82.0%	**96.3%**	**96.7%**
Chen *et al.* [31]	65.0%	76.6%	–	–
Bi *et al.* [32]	64.5%	73.5%	93.4%	95.8%

C. COMPARISONS WITH REPRESENTATIVE METHODS ON LiTS

For a fair comparison, we tabulate the DSC of some state-of-the-art approaches on the same LiTS dataset in Table 4.

Dice per case shows the average DSC over all 3D volumes and Dice global shows the DSC for a single volume obtained by combining all segmentations [30]. All results can be found in the leaderboard.[6] Clearly, our proposed method (team name: Zpark) is very competitive when compared with other existing methods in terms of both liver segmentation and liver tumor segmentation. For example, H-DenseUNet is a state-of-the-art segmentation method for liver tumor, which ranked the 1st on a lesion segmentation challenge

[6]https://competitions.codalab.org/competitions/17094#results
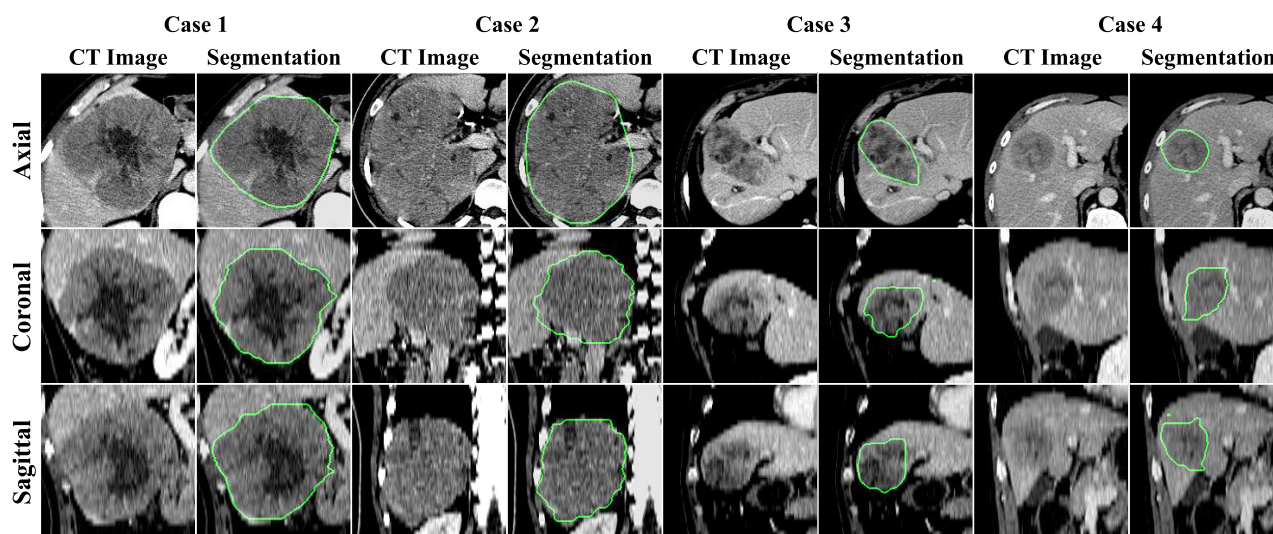
FIGURE 8. Automated tumor segmentation results of representative ISICDM testing data obtained from the proposed method. The green contour denotes the segmentation boundary.

using the MICCAI 2017 LiTS dataset [16]. It reported an average Dice per case of 72.2% and Dice global of 82.4% in terms of tumor segmentation. Our method achieved a better Dice global (84.2%), indicating that our method performed better in cases of larger lesions. It is worth noting that H-DenseUNet is a purely deep learning approach. Incorporating H-DenseUNet into our proposed FCN + level-set pipeline may further enhance our liver and liver tumor segmentation accuracy. From Table 4, it can be observed that 3D CNN [16] typically performes better than 2D CNN [17] in terms of tumor segmentation. All methods under comparison achieved similarly high accuracy on liver segmentation.

V. DISCUSSION

Automatic liver and liver tumor segmentation is an important prior step in computed aided clinical diagnosis. It provides precise contours of liver and any tumor inside the anatomical segment of liver, which is beneficial for doctors in the diagnosis process. In this paper, we presented a deep learning initialized and gradient enhanced level-set segmentation system to combine the advantages of automatic feature extraction in deep learning and interpretable prior knowledge in LSMs. The main advantage of combining those two types of methods is that deep learning can provide a robust initialization for LSMs and LSMs can well guarantee the topology integrity of the outputs. More specifically, LSMs heavily rely on initialization and bad initializations may impair the segmentation, which is one of the main limitations of LSMs. In Fig. 9, we show the segmentation results from our employed level-set method DRLSE with different initializations. Clearly, the proposed initialization method (3D FCN) outputs the best segmentation. The main limitation of purely deep learning methods is that the results may suffer uninterpretable segmentation errors, as shown in Fig. 7.

In terms of computational effort, it will take roughly 90 seconds to segment one whole CT image of size $367 \times 367 \times 45$. For the deep learning part, it will take 10 seconds for 2D U-net to perform coarse liver segmentation and 50 seconds for 3D FCN to localize tumor. The proposed coarse-to-fine strategy can significantly improve the computational efficiency. More specifically, it will take 400 seconds if we use 3D FCN to directly segment the whole CT image but only 60 seconds when using the proposed framework. For the level-set part, it will take 30 seconds to perform FCM and level-set evolution.

Combining deep learning and level-set is one of the research trends in medical image segmentation. For example, Deng *et al.* also proposed a method combining deep learning and level-set in a coarse-to-fine manner and applied their method to liver tumor segmentation from CT images [35]. Compared with existing methods, the proposed one has two main novelties in terms of technical details: (1) we conducted effective image preprocessing via intensity truncation, which is very crucial for both deep learning and level-set based medical image segmentation (see Fig. 10); (2) we used FCM clustering to enhance the edge indicator used in level-set.

To improve the generalization ability of our proposed method and to avoid the over training problem as much as possible, we have adopted data augmentation and eary stopping strateries. We tested our method on two independent datasets to identify the generalization capability of our method in clinical practice. The observed promising segmentation results (Fig. 8 and Table. 4) clearly suggest the great potential of the proposed pipeline in real applications.

A potential limitation of the proposed method is that our liver tumor segmentation performance relied on performance of liver segmentation, given that both FCM and LSM were employed within the liver segmentation mask. For several testing cases in the LiTS dataset, the 3D patch-based liver
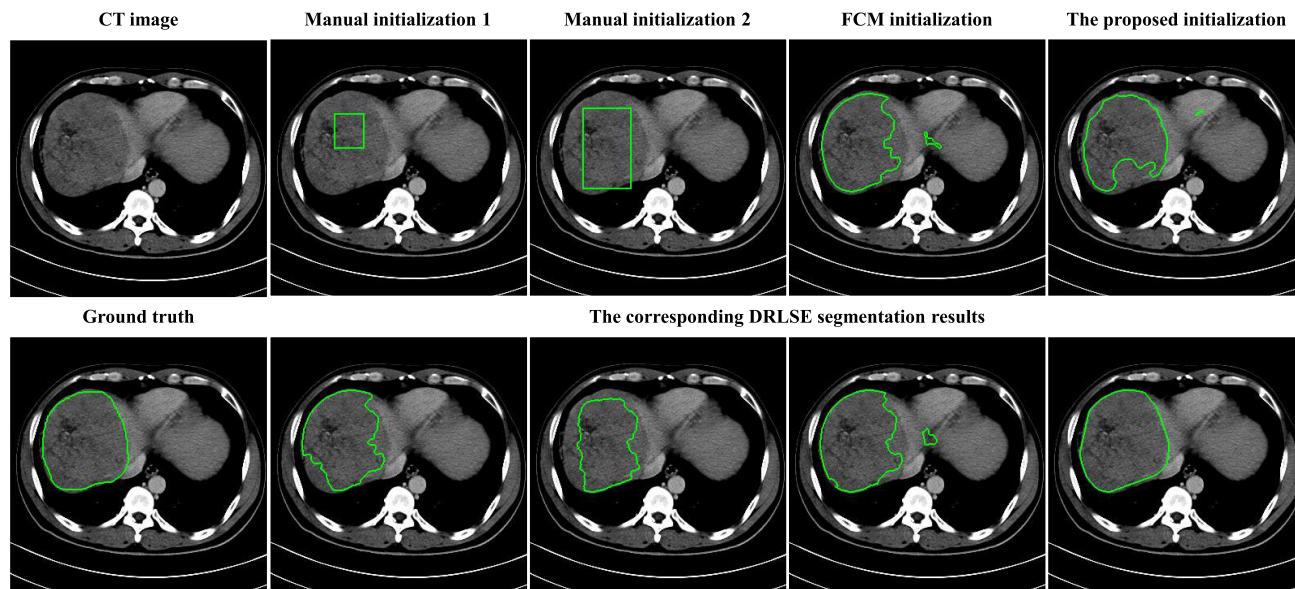
CT image   Manual initialization 1   Manual initialization 2   FCM initialization   The proposed initialization

Ground truth   The corresponding DRLSE segmentation results

FIGURE 9. Four examples to demonstrate the importance of initialization for our employed level-set method DRLSE.

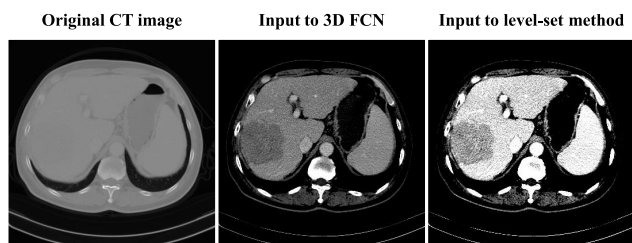Original CT image   Input to 3D FCN   Input to level-set method

FIGURE 10. An example to demonstrate the effectiveness of intensity truncation. The leftmost column denotes the original CT image. The middle column was obtained by a fixed range truncation on the original CT image intensity. The rightmost column was obtained by another intensity truncation based on a range computed from the coarse tumor segmentation from 3D FCN.
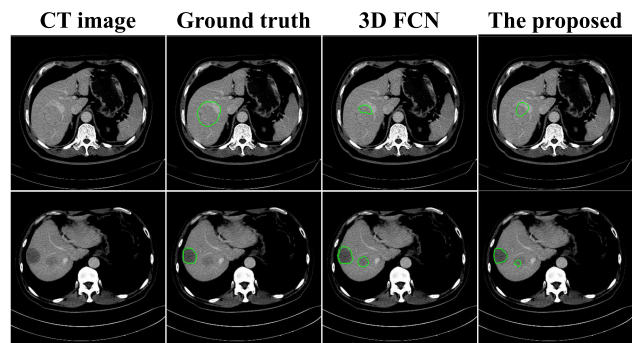

CT image   Ground truth   3D FCN   The proposed

FIGURE 11. False positive and false negative examples.

segmentation was not successful, with holes inside. Those cases can nevertheless be automatically detected through convexity analysis. For those several special cases, we used the 2D slice-based CNN results to be our liver segmentation results. A potential solution is to incorporate atlas-based segmentation methods to preserve liver's topology integrity and this will be one of our future research endeavors [49], [50]. In addition, the proposed method may fail for cases with very fuzzy boundaries, as shown in Fig. 11. These boundaries are very fuzzy because of noises inside CT images. Some denoising methods may be helpful to remove these false positive and false negative issues. For example, the edge-enhancing diffusion filtering technique proposed in [25] may help further enhance the segmentation ability of our proposed pipeline.

VI. CONCLUSION

In this paper, we proposed and validated a novel level-set framework for automatically localizing liver tumor by jointly utilizing deep learning and enhanced edge indication from unsupervised fuzzy c-means. A 2D U-net and a 3D FCN were cascaded to generate liver segmentation at first. Meanwhile, the 3D FCN was also used to roughly localize liver tumor. Both qualitative and quantitative analyses revealed an outstanding performance of the proposed segmentation pipeline.

ACKNOWLEDGMENT

REFERENCES
[1] H. Wang, X. Liang, G. Gravot, C. A. Thorling, D. H. G. Crawford, Z. P. Xu, X. Liu, and M. S. Roberts, "Visualizing liver anatomy, physiology and pharmacology using multiphoton microscopy," *J. Biophotonics*, vol. 10, no. 1, pp. 46–60, Jan. 2017.

[2] F. Bray, J. Ferlay, I. Soerjomataram, R. L. Siegel, L. A. Torre, and A. Jemal, "Global cancer statistics 2018: GLOBOCAN estimates of incidence and mortality worldwide for 36 cancers in 185 countries," *CA, A Cancer J. Clin.*, vol. 68, no. 6, pp. 394–424, Nov. 2018.

[3] D. Wei, S. Ahmad, J. Huo, W. Peng, Y. Ge, Z. Xue, P.-T. Yap, W. Li, D. Shen, and Q. Wang, "Synthesis and inpainting-based MR-CT registration for image-guided thermal ablation of liver tumors," in *Proc. Int. Conf. Med. Image Comput. Comput.-Assist. Intervent.* Cham, Switzerland: Springer, 2019, pp. 512–520.

[4] C. H. Crane and E. J. Koay, "Solutions that enable ablative radiotherapy for large liver tumors: Fractionated dose painting, simultaneous integrated protection, motion management, and computed tomography image guidance," *Cancer*, vol. 122, no. 13, pp. 1974–1986, Jul. 2016.

[5] P. Lamata, F. Lamata, V. Sojar, P. Makowski, L. Massoptier, S. Casciaro, W. Ali, T. Stüdeli, J. Declerck, O. J. Elle, and B. Edwin, "Use of the resection map system as guidance during hepatectomy," *Surgical Endoscopy*, vol. 24, no. 9, pp. 2327–2337, Sep. 2010.

[6] S. Zhang, Y. Zhan, M. Dewan, J. Huang, D. N. Metaxas, and X. S. Zhou, "Towards robust and effective shape modeling: Sparse shape composition," *Med. Image Anal.*, vol. 16, no. 1, pp. 265–277, Jan. 2012.

[7] C. Shi, Y. Cheng, J. Wang, Y. Wang, K. Mori, and S. Tamura, "Low-rank and sparse decomposition based shape model and probabilistic atlas for automatic pathological organ segmentation," *Med. Image Anal.*, vol. 38, pp. 30–49, May 2017.

[8] R. Beichel, C. Bauer, A. Bornik, E. Sorantin, and H. Bischof, "Liver segmentation in CT data: A segmentation refinement approach," in *Proc. 3D Segmentation Clin., Grand Challenge*, 2007, pp. 235–245.

[9] Y. Boykov and G. Funka-Lea, "Graph cuts and efficient N-D image segmentation," *Int. J. Comput. Vis.*, vol. 70, no. 2, pp. 109–131, Nov. 2006.

[10] R. Susomboon, D. S. Raicu, and J. Furst, "A hybrid approach for liver segmentation," in *Proc. MICCAI Workshop 3D Segmentation Clin., Grand Challenge*, 2007, pp. 151–160.

[11] M. Moghbel, S. Mashohor, R. Mahmud, and M. I. B. Saripan, "Review of liver segmentation and computer assisted detection/diagnosis methods in computed tomography," *Artif. Intell. Rev.*, vol. 50, no. 4, pp. 497–537, Dec. 2018.

[12] Y. Zhang, J. Wu, W. Chen, Y. Chen, and X. Tang, "Prostate segmentation using Z-Net," in *Proc. IEEE 16th Int. Symp. Biomed. Imag. (ISBI)*, Apr. 2019, pp. 11–14.

[13] J. Wu, Y. Zhang, and X. Tang, "A multi-atlas guided 3D fully convolutional network for MRI-based subcortical segmentation," in *Proc. IEEE 16th Int. Symp. Biomed. Imag. (ISBI)*, Apr. 2019, pp. 705–708.

[14] G. Chlebus, A. Schenk, J. H. Moltz, B. van Ginneken, H. K. Hahn, and H. Meine, "Automatic liver tumor segmentation in CT with fully convolutional neural networks and object-based postprocessing," *Sci. Rep.*, vol. 8, no. 1, pp. 1–7, Dec. 2018.

[15] Q. Dou, L. Yu, H. Chen, Y. Jin, X. Yang, J. Qin, and P.-A. Heng, "3D deeply supervised network for automated segmentation of volumetric medical images," *Med. Image Anal.*, vol. 41, pp. 40–54, Oct. 2017.

[16] X. Li, H. Chen, X. Qi, Q. Dou, C.-W. Fu, and P.-A. Heng, "H-DenseUNet: Hybrid densely connected UNet for liver and tumor segmentation from CT volumes," *IEEE Trans. Med. Imag.*, vol. 37, no. 12, pp. 2663–2674, Dec. 2018.

[17] E. Vorontsov, A. Tang, C. Pal, and S. Kadoury, "Liver lesion segmentation informed by joint liver segmentation," in *Proc. IEEE 15th Int. Symp. Biomed. Imag. (ISBI)*, Apr. 2018, pp. 1332–1335.

[18] Y. Yuan, "Hierarchical convolutional-deconvolutional neural networks for automatic liver and tumor segmentation," 2017, *arXiv:1710.04540*. [Online]. Available: http://arxiv.org/abs/1710.04540

[19] B. N. Li, C. K. Chui, S. Chang, and S. H. Ong, "A new unified level set method for semi-automatic liver tumor segmentation on contrast-enhanced CT images," *Expert Syst. Appl.*, vol. 39, no. 10, pp. 9661–9668, Aug. 2012.

[20] M. Goetz, E. Heim, K. Maerz, T. Norajitra, M. Hafezi, N. Fard, A. Mehrabi, M. Knoll, C. Weber, L. Maier-Hein, and K. H. Maier-Hein, "A learning-based, fully automatic liver tumor segmentation pipeline based on sparsely annotated training data," *Proc. SPIE*, vol. 9784, Mar. 2016, Art. no. 97841I.

[21] Y. Häme and M. Pollari, "Semi-automatic liver tumor segmentation with hidden Markov measure field model and non-parametric distribution estimation," *Med. Image Anal.*, vol. 16, no. 1, pp. 140–149, Jan. 2012.

[22] A. Hoogi, C. F. Beaulieu, G. M. Cunha, E. Heba, C. B. Sirlin, S. Napel, and D. L. Rubin, "Adaptive local window for level set segmentation of CT and MRI liver lesions," *Med. Image Anal.*, vol. 37, pp. 46–55, Apr. 2017.

[23] C. Li, X. Wang, S. Eberl, M. Fulham, Y. Yin, J. Chen, and D. D. Feng, "A likelihood and local constraint level set model for liver tumor segmentation from CT volumes," *IEEE Trans. Biomed. Eng.*, vol. 60, no. 10, pp. 2967–2977, Oct. 2013.

[24] C. Li, C. Xu, C. Gui, and M. D. Fox, "Distance regularized level set evolution and its application to image segmentation," *IEEE Trans. Image Process.*, vol. 19, no. 12, pp. 3243–3254, Dec. 2010.

[25] O. I. Alirr, A. A. A. Rahni, and E. Golkar, "An automated liver tumour segmentation from abdominal CT scans for hepatic surgical planning," *Int. J. Comput. Assist. Radiol. Surg.*, vol. 13, no. 8, pp. 1169–1176, Aug. 2018.

[26] O. I. Alirr and A. A. A. Rahni, "Automatic liver segmentation from CT scans using intensity analysis and level-set active contours," *J. Eng. Sci. Technol.*, vol. 13, no. 11, pp. 3821–3839, 2018.

[27] T. F. Chan and L. A. Vese, "Active contours without edges," *IEEE Trans. Image Process.*, vol. 10, no. 2, pp. 266–277, Feb. 2001.

[28] N. Paragios and R. Deriche, "Geodesic active regions and level set methods for supervised texture segmentation," *Int. J. Comput. Vis.*, vol. 46, no. 3, pp. 223–247, 2002.

[29] D. Smeets, D. Loeckx, B. Stijnen, B. De Dobbelaer, D. Vandermeulen, and P. Suetens, "Semi-automatic level set segmentation of liver tumors combining a spiral-scanning technique with supervised fuzzy pixel classification," *Med. Image Anal.*, vol. 14, no. 1, pp. 13–20, Feb. 2010.

[30] P. Bilic *et al.*, "The liver tumor segmentation benchmark (LiTS)," 2019, *arXiv:1901.04056*. [Online]. Available: http://arxiv.org/abs/1901.04056

[31] X. Chen, R. Zhang, and P. Yan, "Feature fusion encoder decoder network for automatic liver lesion segmentation," in *Proc. IEEE 16th Int. Symp. Biomed. Imag. (ISBI)*, Apr. 2019, pp. 430–433.

[32] L. Bi, J. Kim, A. Kumar, and D. Feng, "Automatic liver lesion detection using cascaded deep residual networks," 2017, *arXiv:1704.02703*. [Online]. Available: http://arxiv.org/abs/1704.02703

[33] H. Seo, C. Huang, M. Bassenne, R. Xiao, and L. Xing, "Modified U-Net (mU-Net) with incorporation of object-dependent high level features for improved liver and liver-tumor segmentation in CT images," *IEEE Trans. Med. Imag.*, early access, Oct. 18, 2019, doi: 10.1109/TMI.2019.2948320.

[34] H. Jiang, T. Shi, Z. Bai, and L. Huang, "AHCNet: An application of attention mechanism and hybrid connection for liver tumor segmentation in CT volumes," *IEEE Access*, vol. 7, pp. 24898–24909, 2019.

[35] Z. Deng, Q. Guo, and Z. Zhu, "Dynamic regulation of level set parameters using 3D convolutional neural network for liver tumor segmentation," *J. Healthcare Eng.*, vol. 2019, pp. 1–17, Feb. 2019.

[36] O. M. Alia, R. Mandava, and M. E. Aziz, "A hybrid harmony search algorithm for MRI brain segmentation," *Evol. Intell.*, vol. 4, no. 1, pp. 31–49, Mar. 2011.

[37] H. R. Roth, L. Lu, A. Farag, H.-C. Shin, J. Liu, E. B. Turkbey, and R. M. Summers, "DeepOrgan: Multi-level deep convolutional networks for automated pancreas segmentation," in *Proc. Int. Conf. Med. Image Comput. Comput.-Assist. Intervent.* Cham, Switzerland: Springer, 2015, pp. 556–564.

[38] Y. Zhou, L. Xie, W. Shen, Y. Wang, E. K. Fishman, and A. L. Yuille, "A fixed-point model for pancreas segmentation in abdominal CT scans," in *Proc. Int. Conf. Med. Image Comput. Comput.-Assist. Intervent.* Cham, Switzerland: Springer, 2017, pp. 693–701.

[39] R. Vivanti, A. Szeskin, N. Lev-Cohain, J. Sosna, and L. Joskowicz, "Automatic detection of new tumors and tumor burden evaluation in longitudinal liver CT scan studies," *Int. J. Comput. Assist. Radiol. Surg.*, vol. 12, no. 11, pp. 1945–1957, Nov. 2017.

[40] E. Kuntz and H. D. Kuntz, *Hepatology, Principles and Practice: History, Morphology, Biochemistry, Diagnostics, Clinic, Therapy*. Springer, 2006.

[41] F. Isensee and K. H. Maier-Hein, "An attempt at beating the 3D U-Net," 2019, *arXiv:1908.02182*. [Online]. Available: http://arxiv.org/abs/1908.02182

[42] J. Dolz, C. Desrosiers, and I. B. Ayed, "3D fully convolutional networks for subcortical segmentation in MRI: A large-scale study," *NeuroImage*, vol. 170, pp. 456–470, Apr. 2018.

[43] L. Ruskó, G. Bekes, and M. Fidrich, "Automatic segmentation of the liver from multi- and single-phase contrast-enhanced CT images," *Med. Image Anal.*, vol. 13, no. 6, pp. 871–882, Dec. 2009.

[44] K. Liu, Y. Li, X. Hu, M. Lucu, and W. D. Widanage, "Gaussian process regression with automatic relevance determination kernel for calendar aging prediction of lithium-ion batteries," *IEEE Trans. Ind. Informat.*, vol. 16, no. 6, pp. 3767–3777, Jun. 2020.

[45] K. Liu, X. Hu, Z. Wei, Y. Li, and Y. Jiang, "Modified Gaussian process regression models for cyclic capacity prediction of lithium-ion batteries," *IEEE Trans. Transport. Electrific.*, vol. 5, no. 4, pp. 1225–1236, Dec. 2019.

[46] T. Heimann, B. Van Ginneken, M. A. Styner, Y. Arzhaeva, V. Aurich, C. Bauer, A. Beck, C. Becker, R. Beichel, and G. Bekes, "Comparison and evaluation of methods for liver segmentation from CT datasets," *IEEE Trans. Med. Imag.*, vol. 28, no. 8, pp. 1251–1265, Feb. 2009.

[47] Z. Zhu, Y. Xia, W. Shen, E. Fishman, and A. Yuille, "A 3D coarse-to-fine framework for volumetric medical image segmentation," in *Proc. Int. Conf. 3D Vis. (3DV)*, Sep. 2018, pp. 682–690.

[48] Z. Zheng, X. Zhang, H. Xu, W. Liang, S. Zheng, and Y. Shi, "A unified level set framework combining hybrid algorithms for liver and liver tumor segmentation in CT images," *BioMed Res. Int.*, vol. 2018, pp. 1–26, Aug. 2018.

[49] X. Tang, K. Oishi, A. V. Faria, A. E. Hillis, M. S. Albert, S. Mori, and M. I. Miller, "Bayesian parameter estimation and segmentation in the multi-atlas random orbit model," *PLoS ONE*, vol. 8, no. 6, 2013, Art. no. e65591.

[50] J. Wu, Y. Zhang, and X. Tang, "A joint 3D+2D fully convolutional framework for subcortical segmentation," in *Proc. Int. Conf. Med. Image Comput. Comput.-Assist. Intervent.* Cham, Switzerland: Springer, 2019, pp. 301–309.

DONGCEN JI received the B.S degree in electronic information engineering from the Harbin Institute of Technology, in 2018. He is currently pursuing the M.S. degree in electrical and electronic engineering with the Southern University of Science and Technology (joint with the Harbin Institute of Technology). His research interests include medical MRI analysis and image registration.

YUE ZHANG (Graduate Student Member, IEEE) received the B.S. degree in communication engineering from the Southern University of Science and Technology (SUSTech), in 2016. He is currently pursuing the Ph.D. degree in electrical and electronic engineering with The University of Hong Kong (joint with SUSTech), Hong Kong. He has published nine conference papers, including MICCAI, ISBI, IJCNN, and EMBC in related areas. His research interests include medical image segmentation and reconstruction.

YILONG LIU received the B.S. degree in biomedical engineering from the Huazhong University of Science and Technology, Wuhan, China, in 2010, the M.S. degree in biomedical engineering from Tsinghua University, Beijing, China, in 2013, and the Ph.D. degree in electrical and electronic engineering from The University of Hong Kong, in 2018. He is currently a Postdoctoral Fellow in electrical and electronic engineering from The University of Hong Kong. His research interests include MR image reconstruction, MR parallel imaging, MRI motion correction, artifact correction for echo-planar imaging, and functional MRI.

BENXIANG JIANG received the B.S. degree in biomedical engineering from the Southern University of Science and Technology (SUSTech), in 2018. He is currently pursuing the M.S. degree in electrical and electronic engineering with SUSTech (joint with the Harbin Institute of Technology). His research interests include medical image segmentation and level set evolution.

YIFAN CHEN (Senior Member, IEEE) received the B.Eng. (Hons.) and Ph.D. degrees in electrical and electronic engineering from Nanyang Technological University, Singapore, in 2002 and 2006, respectively.

From 2005 to 2007, he was a Project Officer and a Research Fellow with the Singapore-University of Washington Alliance in bioengineering, supported by the Singapore Agency for Science, Technology and Research, Nanyang Technological University, and the University of Washington at Seattle, USA. From 2007 to 2012, he was a Lecturer and a Senior Lecturer with the University of Greenwich and Newcastle University, U.K. From 2012 to 2016, he was a Professor and the Head of the Department of Electrical and Electronic Engineering, Southern University of Science and Technology, Shenzhen, China, appointed through the Recruitment Program of the Global Experts (Thousand Talents Plan). In 2013, he was a Visiting Professor with the Singapore University of Technology and Design, Singapore. He is currently a Professor of engineering and the Associate Dean External Engagement with the Faculty of Science and Engineering and the Faculty of Computing and Mathematical Sciences, The University of Waikato, Hamilton, New Zealand. His current research interests include electromagnetic medical imaging and diagnosis, transient communication with application to healthcare, touchable communication and computation with application to targeted drug delivery, contrast-enhanced medical imaging, fundamentals and applications of nanoscale and molecular communications, and channel modeling for next-generation wireless systems and networks. He is a Fellow of the Institution of Engineering and Technology. He is a Coordinator with the European FP7 CoNHealth Project on intelligent medical ICT, a Group Co-Leader with the European COST Action TD1301 MiMed Project on microwave medical imaging, and an Advisory Committee Member with the European Horizon 2020 CIRCLE Project on molecular communications.

JIONG WU received the B.S. degree in information and computing science and the M.S. degree in computer technology from Lanzhou University, Lanzhou, China, in 2013 and 2016, respectively. He is currently pursuing the Ph.D. degree with the School of Electronics and Information Technology, Sun Yat-sen University, Guangzhou, China. His research interests include medical image segmentation and registration, MRI analysis, machine learning, and deep learning.

ED X. WU (Fellow, IEEE) was an Associate Professor of radiology and biomedical engineering with Columbia University, New York, where he led the NMR Microimaging Laboratory and a Core Member with the Columbia Integrated Imaging Center. From 1990 to 1998, he was a Lead Technical Member with the Development of the World First 3D Positron Emission Tomography (PET) System and the Ultrahigh Field Magnetic Resonance Imaging (MRI) System, Columbia University. He was a Program Director of the Medical Engineering Program, from 2009 to 2013 and an Associate Dean (Research) with the Faculty of Engineering, HKU, from 2013 to 2016. He is currently a Chair Professor of biomedical engineering and holds Lam Woo Professorship in biomedical engineering with The University of Hong Kong. He is also the Founding Director of the Interdisciplinary Laboratory of Biomedical Imaging and Signal Processing and a Research Director of 3T MRI Unit, HKU. His current research interests include MRI engineering, data acquisition, image reconstruction, and high-field and multimodal MRI for understanding large-scale brain structures and circuits.

Prof. Wu is a Fellow of the International Society for Magnetic Resonance in Medicine (ISMRM), in 2013, the American Institute for Medical and Biological Engineering (AIMBE), in 2011, and the Hong Kong Academy of Engineering Sciences (HKAES), in 2018. He was a President of the Overseas Chinese Society for Magnetic Resonance in Medicine (OCSMRM), from 2016 to 2017. He has served with numerous technical and scientific committees in professional societies, funding agencies and international conferences, including U.S. NIH, Hong Kong RGC, and ITC assessment panels. He was a recipient of the 2009 Outstanding Researcher Award with HKU, the 2012 Croucher Senior Research Fellowship with the Croucher Foundation, and the 2018 Guanghua Engineering Science and Technology Prize (Highest National Award) with the Chinese Academy of Engineering.

He was also a recipient of numerous extramural research grants awarded with the U.S. National Institutes of Health (NIH), the U.S. Defense Advanced Research Projects Agency (DARPA), the U.S. Department of Interior, and the Hong Kong Research Grant Council (RGC). He is the Asia-Pacific Editor of *NMR in Biomedicine* and an Editorial Board Member of *Magnetic Resonance in Medicine*.

XIAOYING TANG (Member, IEEE) received the B.S. degree in control system engineering and foreign language education from the Huazhong University of Science and Technology, Wuhan, China, in 2009, and the M.S. degrees in electrical and computer engineering and applied mathematics and statistics and the Ph.D. degree in electrical and computer engineering from Johns Hopkins University, USA, in 2011, 2014, and 2014, respectively.

From 2014 to 2015, she was a Visiting Professor in electrical and computer engineering with Carnegie Mellon University. From 2015 to 2018, she was a Tenure-track Assistant Professor with the SYSU-CMU Joint Institute of Engineering, Sun Yat-sen University. She is currently an Assistant Professor and an Associate Researcher with the Department of Electrical and Electronic Engineering, Southern University of Science and Technology. Her research interests include medical image segmentation and registration, diffusion tensor image analysis, statistical shape analysis, manifold learning and clustering, spatiotemporal analysis, multimodality MRI analysis, pattern recognition, machine learning, and big data in medicine.

• • •